Quasi-electrostatic whistler mode wave excitation by linear scattering of EM whistler mode waves from magnetic field-aligned density irregularities

F. R. Foust,[1] U. S. Inan,[1,2] T. Bell,[1] and N. G. Lehtinen[1]

Received 22 June 2010; revised 9 August 2010; accepted 13 August 2010; published 10 November 2010.

[1] Recent observations by Starks et al. (2008) from multiple spacecraft suggest that the actual nighttime intensity of VLF transmitter signals in the radiation belts is approximately 20 dB below the level that is assumed in the model developed by Abel and Thorne (1998) and approximately 10 dB below model values during the day. In the present work, we discuss one experimentally established mechanism which might be responsible for some of this intensity discrepancy, linear mode coupling as electromagnetic whistler mode waves propagate through regions containing small-scale (2–100 m) magnetic field-aligned plasma density irregularities. The scattering process excites quasi-electrostatic whistler mode waves, which represents a power loss for the input waves. Although the distribution and amplitude of the irregularities is not well known at present, we construct plausible models in order to use numerical simulations to determine the characteristics of the mode coupling mechanism and the conditions under which the input VLF waves can lose significant power to the excited quasi-electrostatic whistler mode waves. For short propagation paths of approximately 15 km, the full-wave model predicts power losses ranging from −3 dB (25% probability) to −7 dB (2% probability). For longer propagation paths of approximately 150 km, the full-wave model predicts power losses ranging from −4 dB (25% probability) to over −10 dB (2% probability). We conclude that for the irregularity models investigated, the mode coupling mechanism can result in significant power loss for VLF electromagnetic whistler mode waves.

Citation: Foust, F. R., U. S. Inan, T. Bell, and N. G. Lehtinen (2010), Quasi-electrostatic whistler mode wave excitation by linear scattering of EM whistler mode waves from magnetic field-aligned density irregularities, *J. Geophys. Res.*, *115*, A11310, doi:10.1029/2010JA015850.

1. Introduction

[2] The energetic particles comprising the Earth's radiation belts are an important component of Space Weather, and much effort has been expended to understand how these particles are energized during periods of magnetic disturbance, and how the energized particles are eventually precipitated from the belts in the quasi-steady state following the magnetic disturbance. One commonly accepted model of the quasi-steady state radiation belts is that of *Abel and Thorne* [1998] and *Millan and Thorne* [2007]. This model proposes that VLF signals from powerful ground based transmitters determine the lifetimes of energetic radiation belt electrons (100 keV to 1.5 MeV) on L shells in the range 1.3–2.8. The primary mechanism of interaction is pitch angle scattering during gyroresonance, where the resonance condition can be expressed

$$v_z = (m\omega_{ce}/\gamma - \omega)/k_z, \tag{1}$$

where v_z is the component of the electron velocity along $\mathbf{B}_0$ the Earth's magnetic field, m is an integer, ω_{ce} is the electron gyrofrequency, ω is the wave frequency, $\gamma = 1/\sqrt{1 - v^2/c^2}$, c = velocity of light, and k_z is the component of the wave vector $\mathbf{k}$ along $\mathbf{B}_0$. As a result of the pitch angle scattering, energetic electrons are precipitated into the atmosphere at the base of the given L shell in both hemispheres.

[3] Recent observations [*Starks et al.*, 2008] from five spacecraft suggest that the actual nighttime intensity of VLF transmitter signals in the radiation belts is approximately 20 dB below the level that is assumed by *Abel and Thorne* [1998] model and approximately 10 dB below model values during the day. Furthermore, DEMETER plasma wave observations above the NWC VLF transmitter (19.8 kHz) indicated that much of the nominal 20 dB wave intensity decrease occurs as the VLF waves propagate upward between 110 and 700 km [*Lehtinen and Inan*, 2009]. *Starks et al.* [2008] suggested that unmodeled loss processes such

[1]Department of Electrical Engineering, Stanford University, Stanford, California, USA.
[2]Koç University, Rumelifeneri Yolu, Istanbul, Turkey.

0148-0227/10/2010JA015850

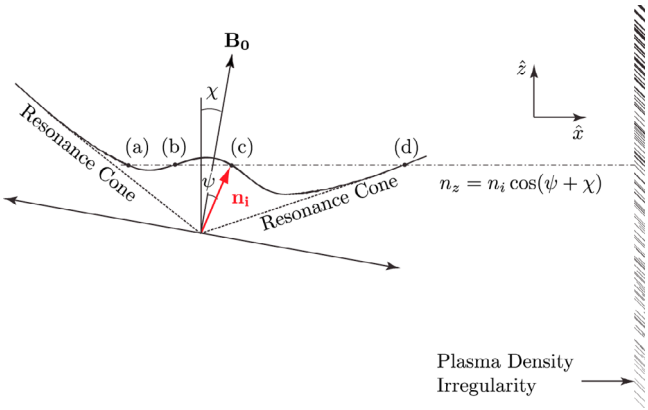

Figure 1. Application of Snell's law to the case of an EM whistler mode wave scattering from a planar plasma density irregularity. It is assumed that the incident wave has a refractive index n_i and its wave normal angle with respect to the ambient magnetic field $\mathbf{B}_0$ has the value ψ. By Snell's law, the component of n_i parallel to the surface of the irregularity, n_z, must be the same for the input wave plus all transmitted and reflected waves. It can be seen that there are four possible solutions. Solutions (c) and (b) are the input and reflected EM whistler mode waves, and (a) and (d) are the transmitted and reflected QE whistler mode waves.

as mode conversion, scattering, or enhanced reflection might be responsible for this discrepancy. Recent observations of upward propagating VLF transmitter signals on the DEMETER spacecraft at ≃700 km altitude have shown that at least one such mode coupling mechanism exists in which VLF transmitter signals scatter linearly from small-scale magnetic field-aligned plasma density irregularities and excite quasi-electrostatic (QE) waves of relatively small wavelength (10–100 m) [*Bell et al.*, 2008]. The excitation process can be understood from a simple application of Snell's law to the case of a whistler mode wave scattering from a planar plasma density irregularity, as detailed in Figure 1, which shows a cross section of the refractive index surface (blue) for an input electromagnetic (EM) whistler mode wave. The refractive index surface is generated by plotting the refractive index $n(\psi)$ as a function of the wave normal angle ψ. It is assumed that the wave vector $\mathbf{k}$ lies in the plane of the paper and that the planar irregularity lies in a plane perpendicular to the plane of the paper. Thus the normal to the planar irregularity also lies in the plane of the paper. The component of the refractive index parallel to the surface of the irregularity is $n_z = n_i(\psi)\cos(\psi + \chi)$, where $n_i(\psi)$ is the refractive index of the input wave and χ is the angle between the ambient magnetic field $\mathbf{B}_0$ and the plane of the irregularity. By Snell's law, n_z must be the same for the input wave plus all transmitted and reflected waves, If we draw the level line n_z = constant, we see from the $n(\psi)$ surface that there are four possible solutions, (a), (b), (c), and (d). Solutions (c) and (b) represent the input EM wave and the reflected EM wave. Solutions (a) and (d) represent reflected and transmitted QE waves. On a spacecraft, the QE waves are easily distinguished from the electromagnetic (EM) input whistler mode waves through their large Doppler shifts (≥50 Hz) [*Bell et al.*, 1983; *Bell and Ngo*, 1988].

[4] Although this particular mode coupling process has now been identified, it is not clear that the VLF transmitter signals which scatter from the small-scale plasma density irregularities will actually lose 20 dB in intensity as they propagate upward to 700 km altitude. For example, once excited through the scattering mechanism, the QE waves can subsequently also scatter from the irregularities and excite new EM whistler mode waves, thus returning energy to the EM waves [*Bell and Ngo*, 1990].

[5] Our purpose in the present paper is to estimate the power loss of EM VLF whistler mode waves while propagating upward to 700 km altitude at midlatitude. We accomplish this task through simulations, as described below.

[6] We first provide some background information and prior work, in which we set the context and provide motivation for the simulations. We discuss what is currently known from spacecraft observations about the size and relative magnitude of the plasma density irregularities. In section 2, we discuss the models used in this paper. We first demonstrate the basic scattering process in section 2.1 via a linearized model based on perturbation theory. This provides reasonable physical constraints on the size and spatial period of the density perturbations, and motivates the development of the full-wave model discussed in section 2.2. We devote the remainder of section 2 to discussion of the physical model, including construction of the incident wave and the plasma density perturbation.

[7] We discuss the results in section 3. We first summarize the results of a simple sinusoidal density perturbation in section 3.1. We then conduct a statistical investigation of more realistic randomized mode sums in section 3.3. In sections 3.4 and 3.5, we again conduct randomized trials to show the role of the coherence length of the density perturbations on the strength and relative likelihood of strong quasi-electrostatic mode conversion.

[8] There is very little known about the origins and characteristics of the small-scale plasma density irregularities which scatter whistler mode waves in the magnetosphere, producing QE whistler mode waves during the scattering process. The irregularities appear to be present at altitudes ranging from 700 to 20,000 km [*Bell et al.*, 2004, 2008] and at magnetic latitudes ranging from approximately 15 to 75 degrees [*Titova et al.*, 1984; *James and Bell*, 1987; *Tanaka et al.*, 1987; *Bell et al.*, 2008] and the scale of the irregularities appears to range from approximately 2 to 100 meters [*Bell et al.*, 1991].

[9] The spatial power spectral density of the irregularities has been inferred in a few cases [*James and Bell*, 1987; *Bell et al.*, 1991]. For example, multiple antenna observations on the DE-1 spacecraft of Doppler shifts in fixed frequency pulses from ground based VLF transmitters suggested that the k-space power spectral density of the Doppler shifted waves has the form:

$$P_{sd}(k) \simeq 0.3(k/k_0)^2 e^{-k^2/k_0^2}(mV)^2, \qquad (2)$$

where k_0 = 0.22/m. Since the wavelength of the scattered waves is comparable to the spatial wavelength of the small-scale plasma density irregularities, (2) may also represent the range of the spatial wavelengths of the irregularities. Accord-

ing to (2), the two −10 dB points of the distribution occur at ≃13 m and 130 m, and it can be assumed that the spatial wavelength of the irregularities covers the same range.

[10] It is possible that some of the small-scale irregularities may be associated with slowly propagating plasma waves with relatively small frequencies [*Titova et al.*, 1984; *Groves et al.*, 1988]. In the *Titova et al.* [1984] mechanism the frequency shifted waves are produced by nonlinear mode coupling between an EM whistler mode wave and an ion acoustic wave. The ion acoustic wave provides the plasma density structure from which the EM waves scatter. This mechanism results in a true frequency shift of the input EM whistler mode wave. The free energy source for this model is assumed to derive from local precipitating particle beams. Since the maximum frequency shift of the EM wave is equal to the ion gyrofrequency, this particular mechanism cannot explain the frequency shifts of 1 kHz or more observed on a number of spacecraft.

[11] Observations from the DEMETER spacecraft have shown a strong correlation between general plasma density irregularities and excited QE whistler mode waves [*Bell et al.*, 2008]. However since the plasma density is measured only once per second and the spacecraft travels at ≃7 km/s, any correlation between excited QE waves and small-scale plasma density irregularities could not be established. In fact, the plasma density would need to be measured at a rate of 2000 samples per second in order to resolve irregularities with a spatial wavelength as small as 7 m.

[12] These satellite observations and prior work allow us to make reasonable inferences on the bounds of the magnitude and characteristic length scale of the plasma density irregularities. However, since the exact details and fine-scale structure of the plasma density irregularities are not known, we are motivated to develop a computational model to investigate precisely what properties of a plasma density irregularity can give rise to strong scattering of incident whistler mode waves into quasi-electrostatic whistler mode waves. The remainder of this paper is devoted to this investigation. We begin by deriving a model based on perturbation theory to show the basic physical mechanism of the scattering process.

2. Models

[13] The electromagnetic fields associated with an electromagnetic wave of frequency ω propagating within a cold magnetoplasma can be characterized through Maxwell's equations:

$$\nabla \times E(r) = -i\omega B(r), \tag{3}$$

$$\nabla \times B(r) = \frac{i\omega}{c^2}\overline{K}E(r), \tag{4}$$

where $E(r)$ and $B(r)$ are, respectively, the vector electric and magnetic fields of the propagating wave, r is the position vector of the observation point, ω is the wave frequency, c is the speed of light, and the dielectric tensor $\overline{K}$ has the value:

$$\overline{K} = \begin{pmatrix} S & iD & 0 \\ -iD & S & 0 \\ 0 & 0 & P \end{pmatrix}, \tag{5}$$

where the Earth's magnetic field $\mathbf{B}_0$ is directed along the z axis, and where the dielectric constants S, D, and P are the plasma parameters defined by *Stix* [1962], page 10 for a cold multicomponent plasma. An important feature of the tensor $\overline{K}$ is the fact that the diagonal dielectric constant P is always negative for the frequency range considered in the present paper. This insures that a refractive index resonance cone will exist as long as the other diagonal dielectric constant S is positive, as it will be for all $f_{ce} \geq f \geq f_{lhr}$, where f_{lhr} is the lower hybrid resonance frequency.

[14] The components of $\overline{K}$ are related to the local plasma parameters for a multicomponent plasma as

$$\begin{aligned} R &= 1 - \sum_s \frac{\omega_{ps}^2}{\omega(\omega + \omega_{cs})} \\ L &= 1 - \sum_s \frac{\omega_{ps}^2}{\omega(\omega - \omega_{cs})} \\ P &= 1 - \sum_s \frac{\omega_{ps}^2}{\omega^2} \\ S &= \frac{1}{2}(R + L) \\ D &= \frac{1}{2}(R - L) \end{aligned} \quad ,$$

where ω_{ps} is the local plasma frequency for each species s, ω_{cs} is the local (signed) gyrofrequency for each species s, and ω is the wave frequency. Equations (3) and (4) can be combined to yield the wave equation for waves propagating in the magnetoplasma,

$$\nabla \times \nabla \times E(r) - \beta_0^2 \overline{K}E(r) = 0, \tag{6}$$

where $\beta_0 = \omega/c$.

[15] Because the field components are coupled through the dielectric tensor, (6) represents a fourth-order differential equation for each component of $E(r)$. Thus there are four separate wave modes which can exist in the medium. Assuming that $f_{pe} > f_{ce}$ and $f_{ci} \leq f \leq f_{ce}$, the only two propagating modes are right-hand-polarized whistler mode waves; the two left-hand-polarized modes are evanescent.

2.1. Perturbation Model

[16] In our perturbation model we are interested in whistler mode waves which propagate through regions containing small-scale electron density irregularities. We express the electron density in the form:

$$N(r) = N_0 + \delta N_0(r), \tag{7}$$

where N_0 is the average value of $N(r)$, $\delta N_0(r)$ represents the density perturbation, and $|\delta N_0(r)/N_0| \ll 1$.

[17] Noting that $f_{pe}^2 = \frac{e^2}{m\varepsilon_0}[N_0 + \delta N_0(r)]/(2\pi)^2$, we can express (6) in the following way:

$$\nabla \times \nabla \times E(r) - \beta_0^2 \overline{K_0}E(r) = \beta_0^2 \frac{\delta N_0(r)}{N_0}\overline{K_1}E(r), \tag{8}$$

where $\overline{K_0}$ is the average value of $\overline{K}$ in the region of irregularities and $\overline{K_1} = \overline{K_0} - \overline{I}$, where $\overline{I}$ is the identity matrix.

[18] We now assume an input whistler mode wave is incident upon the irregularity region. The total wavefield is $E_i(r) + E_s(r)$, where $E_i(r)$ is the electric field of the input

wave and $E_s(r)$ is the electric field of the scattered wave. The field $E_i(r)$ is the solution to (6) when the right-hand side is set equal to zero. For now, we will assume for a moment that the scattered wave amplitude is much smaller than that of the input wave. This cannot hold in the general case, but it provides useful insight into the scattering process. We will discuss the full implications of this assumption later, which will motivate the use of the more general full-wave model developed in the next section. If this assumption holds, that is, $|E_s(r)| \ll |E_i(r)|$, then the first-order approximation of (6) will be

$$\nabla \times \nabla \times E_s(r) - \beta_0^2 \overline{K_0} E_s(r) = \beta_0^2 \frac{\delta N_0(r)}{N_0} \overline{K_1} E_i(r). \quad (9)$$

Since the rhs of (9) is a known function of r, the equation can in principle be solved to find $E_s(r)$. To illustrate the predictions of (9), we consider the very simple case in which the irregularities vary only along the x axis and the wave vector $\mathbf{k_i}$ of the input wave lies in the x-z plane. In this case the 4 modes which make up the solution of (9) can be uncoupled [*Ngo*, 1989] to yield the expression for $E_{sx}(x)$:

$$\left(\frac{d^2}{dx^2} + k_{x1}^2\right)\left(\frac{d^2}{dx^2} + k_{x2}^2\right) E_{sx}(x) = \sum_l \sum_\nu Q_\nu^{xl} E_{il} \frac{d^\nu}{dx^\nu} \cdot \left[\eta(x) e^{-i(k_{ix}x + k_{iz}z)}\right], \quad (10)$$

where we have assumed that the input wave is planar with the form $\mathbf{E_i(r)} = [E_{ix}\mathbf{a_x} + E_{iy}\mathbf{a_y} + E_{iz}\mathbf{a_z}]e^{-i(k_{ix}x + k_{iz}z)}$, where $\mathbf{a_{x,y,z}}$ are unit vectors along the x, y, z axes, where l = x, y, z, ν = 0, 1, 2, 3, 4, η(x) = δN_0(x)/N_0, and where

$$\begin{aligned}
k_{x1}^2 &= \beta_0^2\left[\gamma_1 - \sqrt{\gamma_1^2 - \gamma_2^2}\right] \\
k_{x2}^2 &= \beta_0^2\left[\gamma_1 + \sqrt{\gamma_1^2 - \gamma_2^2}\right] \\
\gamma_1 &= \left[P_0 + R_0 L_0/S_0 - n_{iz}^2(1 + P_0/S_0)\right]/2 \\
\gamma_2 &= \left[n_{iz}^4 - 2S_0 n_{iz}^2 + R_0 L_0\right] P_0/S_0 \\
Q_0^{xx} &= \beta_0^4\left[(n_{iz}^2 - S_0)(S_0 - 1) + D_0^2\right] P_0/S_0 \\
Q_2^{xx} &= \beta_0^2\left[D_0^2 + [n_{iz}^2 - S_0 - P_0)](S_0 - 1)\right]/S_0 \\
Q_4^{xx} &= -(S_0 - 1)/S_0 \\
Q_0^{xy} &= i\beta_0^4 P_0 D_0 (n_{iz}^2 - 1)/S_0 \\
Q_2^{xy} &= i\beta_0^2\left[k_{iz}^2 - \beta^2(1 + P_0)\right] D_0/S_0 \\
Q_4^{xy} &= -iD_0/S_0 \\
Q_1^{xz} &= -i\beta_0^3 n_{iz}(n_{iz}^2 - S_0) P_0/S_0 \\
Q_3^{xz} &= i\beta_0 n_{iz} P_0/S_0
\end{aligned}$$

and where $Q_1^{xx} = Q_3^{xx} = Q_1^{xy} = Q_3^{xy} = Q_0^{xz} = Q_2^{xz} = Q_4^{xz} = 0$.

[19] The input wave E field on the rhs of (10) can be either an EM whistler mode wave or a QE whistler mode wave. For present purposes we assume it is an EM whistler mode wave, which when scattered from the plasma density irregularities excites both QE and EM waves. The square of the x axis component of the wave number of the excited QE wave has the value k_{x2}^2 given above, and if the angle ψ between $\mathbf{k_i}$ and $\mathbf{B}_0$ is not large then $k_{x2}^2 \simeq -(P_0/S_0)n_{iz}^2\beta_0^2 \simeq (f_{ce}/f)^2 n_{iz}^2 \beta_0^2$. Thus the refractive index of the QE wave will be larger than the refractive index of the incident EM wave by a factor of f_{ce}/f.

[20] We assume that the variable $\eta(x)$, the normalized density irregularity function, can be expressed as a Fourier series over the region of space, $0 \le x \le d$, assumed to contain the plasma density irregularities:

$$\eta(x) = \sum_{m=-\infty}^{\infty} \eta_m e^{-ik_m x}, \quad (11)$$

where $k_m = 2\pi m/d$.

[21] Since we are interested in the excitation of QE waves for which $\frac{d^2}{dx^2}E_{sx}$; $-k_{x2}^2 E_{sx}$, we can approximate the first term on the lhs of (8) by the factor $k_{x1}^2 - k_{x2}^2$. Then introducing (11) into (10) we arrive at our final expression:

$$\left(\frac{d^2}{dx^2} + k_{x2}^2\right) E_{sx}(x) = \sum_m \sum_l \sum_\nu Q_\nu^{xl} E_{il} \lambda_\nu \left[\eta_m e^{-i(k_{ix} + k_m)x}\right], \quad (12)$$

where $\lambda_\nu = [-i(k_{ix} + k_m)]\nu/(k_{x1}^2 - k_{x2}^2)$ and where the factor $e^{-ik_{iz}z}$ is now included in each field component.

[22] The particular solution to (12) shows that the amplitude of E_{sx} will increase linearly with distance whenever the matching condition obtains: $k_{x2} = \pm[k_m + k_{ix}]$. Since $k_{x2} \gg k_{x1}$, the matching condition corresponds to the case in which the QE whistler mode waves excited in the irregularity region possess a wavelength closely equal to the wavelength of one of the spatial Fourier components of the irregularity distribution. For QE waves propagating in the positive x direction the particular solution of (12) has the form

$$E_{sx}(x) = -\frac{i\eta_n}{2k_{x2}^2} \sum_l \sum_\nu Q_\nu^{xl} E_{il} \lambda_\nu (k_{x2}x) e^{ik_{x2}x}, \quad (13)$$

where η_n is the amplitude of the particular spatial Fourier component of $\eta(x)$ for which $k_{x2} = (k_m + k_{ix})$, and where $0 \le x \le d$.

[23] Equation (13) predicts that the amplitude of the excited QE wave will grow linearly with distance. Thus power in the EM wave readily flows into the QE waves. However, this situation cannot continue indefinitely because as the amplitude of the QE wave grows it will begin to transfer significant wave power back into EM whistler mode waves through the same scattering process. Thus it is clear that the perturbation solution expressed in (12) cannot accurately describe this multiwave scattering process over large distances because the necessary condition, $|E_s| \le |E_i|$, will not be met. In order to understand this multiwave scattering process, we need to turn to the full wave method described below.

2.2. Full-Wave Model

[24] The full-wave model used here is similar to that employed earlier by *Bell and Ngo* [1990] and is described in

detail by *Lehtinen and Inan* [2008]. It is a model in which the plasma density is assumed to vary only along a single axis. The method follows other full-wave methods in that it relies on solving the reflection coefficients for the two EM modes and the two QE modes at the interfaces of homogeneous layers. The work extends prior work in that it solves the resulting system of equations using an efficient, inherently stable recursion relation. In the context of this paper, the primary advantage of the method is the explicit separation of propagating modes in k-space; the field amplitudes for each of the four possible modes are solved explicitly. Further, the method can accommodate any distribution of vertical or horizontal source currents, simplifying the construction of complicated sources.

[25] We slightly deviate from the notation of *Lehtinen and Inan* [2008], swapping coordinates such that $(x, y, z) \rightarrow (y, z, x)$ and defining the conserved component of the refractive index as $\mathbf{n}_{\|}$, but the method is otherwise identical. We first define the refractive index vector $\mathbf{n} = \mathbf{k}c/\omega$. The coordinate system is chosen so that the $\hat{\mathbf{x}}$ axis is normal to the layers. By Snell's law, the parallel component of the refractive index $\mathbf{n}_{\|} = n_y\mathbf{y} + n_z\hat{\mathbf{z}}$ is constant across the boundaries.

[26] When a spatial Fourier transform is applied to (6), one obtains the Booker quartic, which represents the dispersion relation in a magnetoplasma for n_x as a function of n_y and n_z. A graphical solution to the Booker quartic equation for a whistler mode wave in a magnetoplasma is shown in Figure 1. The quartic is solved numerically at each interface, and the four solutions are sorted into forward and backward modes (with respect to the layers) by the sign and magnitude of the normal component of the refractive index vector n_x, yielding a sorted vector $(n_x^{u1}, n_x^{u2}, n_x^{d1}, n_x^{d2})^T$, corresponding to the two forward and two backward propagating modes, respectively. The same sorting is used for the mode amplitudes $(u^1, u^2, d^1, d^2)^T$, which are then solved for in each layer by an efficient recursion relation. Finally, the fields in each layer i are related to the mode amplitudes via a 6×4 matrix $\mathcal{F}_i$:

$$\begin{pmatrix} \mathbf{E}_i(\mathbf{r}) \\ \mathbf{H}_i(\mathbf{r}) \end{pmatrix} = \mathcal{F}_i \begin{pmatrix} u_i^1(x) \\ u_i^2(x) \\ d_i^1(x) \\ d_i^2(x) \end{pmatrix} e^{ik_0(\mathbf{n}_{\|} \cdot \mathbf{r}_{\|})}. \tag{14}$$

The matrix $\mathcal{F}_i$ is constructed by finding the characteristic fields $\mathbf{E}_i$ and $\mathbf{H}_i$ belonging to each mode $n_x^{u1}, n_x^{u2}, n_x^{d1}, n_x^{d2}$ of the Booker quartic in each layer i.

[27] After solving for the mode amplitudes, the field amplitudes for a specific mode can then be extracted by setting the other mode amplitudes equal to zero, e.g., supposing we want only the fields associated with the backward mode d^1, we would use the mode amplitude vector $(0, 0, d^1, 0)^T$.

[28] Quasi-electrostatic whistler mode waves are defined as those for which the wave electric field is nearly parallel to the wavenormal, that is, $|E_{\|}| \gg |E_{\perp}|$. For whistler mode waves propagating with wave frequency above the lower hybrid resonance frequency, this will occur in the short-wavelength limit as the refractive index approaches infinity along the resonance cone. For the purposes of this paper, we will refer to EM whistler mode waves as those propagating with Ψ less than the Gendrin angle, and QE whistler mode waves as those with Ψ greater than the Gendrin angle, where the Gendrin angle is defined as the nonzero angle Ψ at which the group velocity vector is parallel to the background magnetic field B_0.

[29] For a lossless or mildly lossy medium, the group velocity vectors are coincident with the direction of the time-harmonic Poynting vector,

$$\mathbf{S} = \frac{1}{2}\Re\{\mathbf{E} \times \mathbf{H}^*\}. \tag{15}$$

The quantity of interest used throughout this paper is the power conversion ratio, that is, the ratio of the normal component of reflected or transmitted Poynting flux to the normal component of the incident Poynting flux, which indicates how much power in a particular incident whistler mode wave mode is reflected, transmitted, or converted into QE waves.

[30] We note that accurate measurement of the electric field using a dipole antenna in a magnetoplasma is a difficult problem. Indeed, attempts to characterize the behavior of a spaceborne antenna of length L in a magnetoplasma in terms of an "effective" antenna length have yielded many different values, including $L/2$ [*Imachi et al.*, 2000], L [*Sonwalkar and Inan*, 1986], and even $30L$ for propagation near the resonance cone [*James*, 2006]. Provided, however, that the accurate estimates of the electric field are available, then a method such as that described by *Santolík et al.* [2003] can be used to estimate the wavenormal direction and wave power from even incomplete magnetic and electric field measurements, to which our results can be directly applied.

2.3. Scattering Problem

[31] We restrict our discussion to the scattering of beams of whistler mode waves off small-scale magnetic field-aligned density irregularities, represented by uniform slabs, infinite in transverse extent.

[32] It is well known that for small amplitude periodic densitity irregularities, the power in the scattered signal is maximized when the matching condition holds [*Harker and Crawford*, 1969]

$$\overrightarrow{k_i} + \overrightarrow{k} = \overrightarrow{k_s}, \tag{16}$$

where $\overrightarrow{K_i}$ is the wave vector of the incident wave, $\vec{k}$ is the characteristic wave vector of the perturbation, and $\overrightarrow{k_s}$ is the wave vector of the scattered signal. In a magnetoplasma at frequencies above f_{lhr}, the QE mode's wavelength will generally be much smaller than that of the incident whistler mode wave, which implies that we can maximize conversion of whistler mode energy into the QE mode if the characteristic scale of the density irregularities is approximately equal to the that of the normal component of the k-vector of the QE mode we wish to excite, that is,

$$k_x \approx k_{x,\mathrm{QE}}. \tag{17}$$

Implicit in applying this matching condition to linear scattering off plasma density irregularities is the fact that the density perturbation must be kept small, on the order of a few percent. For large perturbations, a simple matching condition like this no longer applies; matching is effectively destroyed by the large changes in refractive index.

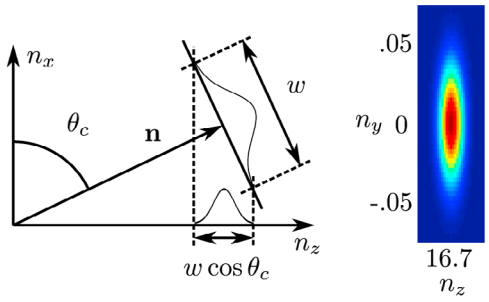

Figure 2. Illustration showing the construction of a Gaussian beam in refractive index-space (normalized k-space). The width w is the effective width of the beam in refractive index-space. The angle of incidence of the center of the beam with respect to the normal to the scattering layers is θ_c. The projection onto the parallel refractive index surface components yields the Gaussian window used to weight the source currents. (right) The window in parallel refractive index space.

2.4. Gaussian Whistler Mode Beam

[33] Since the whistler mode waves from a ground based source will not possess planar wavefronts, the incident wave is constructed as a pseudo-Gaussian whistler mode beam, with a finite effective width and centered about a central angle θ_c, where θ is the angle of incidence. We construct the beam by finding the equivalent source currents in k-space for a series of whistler mode plane waves clustered about θ_c. Choosing the first layer in the medium as a source layer, the plane waves can be related to equivalent electric surface currents $\mathbf{J}_s$ and magnetic surface currents $\mathbf{M}_s$ [*Balanis*, 1989]:

$$\mathbf{J}_s = \hat{\mathbf{n}} \times \mathbf{H}, \tag{18}$$

$$\mathbf{M}_s = -\hat{\mathbf{n}} \times \mathbf{E}, \tag{19}$$

where $\hat{\mathbf{n}}$ is the normal to the layers.

[34] To proceed, we assume that the wavenormals of the incident whistler mode beam are confined to a narrow cone about a central angle θ_c and that the variation in the magnitude of $\vec{k}$ as a function of propagation angle is small within the narrow cone. This allows us to project a Gaussian window onto the n_y-n_z plane as shown in Figure 2, and then weight the source currents with this window. We restrict ourselves to relatively wide beams, because at narrow widths relative to the wavelength, the beam can be significantly diffracted as it propagates. In this paper we use a 200 km wide beam, sufficiently wide at these frequencies so that the beam can propagate for many thousands of kilometers with minimal spread due to diffraction.

2.5. Simple Density Profile

[35] A simple electron number density profile as a function of distance along the z axis is shown in Figure 3. This profile can be envisioned as one of the spatial Fourier components of (9). N_L is the number of sinusoidal periods in the irregularity, N_0 is the background electron number density, and δN_0 is the perturbation factor; positive values represent an enhancement, and negative represent a depletion. The characteristic length scale λ is perturbed by a factor κ in order to investigate the sensitivity of the mode conversion efficiency to the period of the density perturbation.

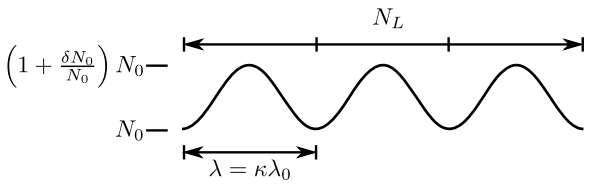

Figure 3. Electron number density for a typical periodic scattering structure as a function of the distance along the normal $\hat{x}$ to the scatttering layers.

3. Results

[36] We define the mode conversion efficiency as the ratio of the normal component of the Poynting flux for a particular mode to the normal component of the Poynting flux for the incident whistler mode wave. For the forward-scattered (with respect to the layers) QE mode, $\alpha_{\mathrm{QE,f}} = S_{x,\mathrm{QE,f}}/S_{x,\mathrm{inc}}$, and for the backward-scattered QE mode, $\alpha_{\mathrm{QE,b}} = -S_{x,\mathrm{QE,b}}/S_{x,\mathrm{inc}}$.

[37] Quasi-electrostatic mode excitation is most likely to be observed at night when ionospheric absorption is low. As such, all simulations are run using a typical nighttime plasma electron and ion number density taken from DEMETER observations at midlatitudes at approximately 700 km altitude. The plasma parameters are assumed to be

$$f_{\mathrm{wave}} = 20\ \mathrm{kHz} \tag{20}$$

$$f_{\mathrm{ce}} = 635\ \mathrm{kHz}, \tag{21}$$

$$f_{\mathrm{pe}} = 1.87\ \mathrm{MHz}, \tag{22}$$

$$f_{\mathrm{LHR}} = 8.77\ \mathrm{kHz}, \tag{23}$$

$$\psi_{\mathrm{res}} = 88.29^\circ, \tag{24}$$

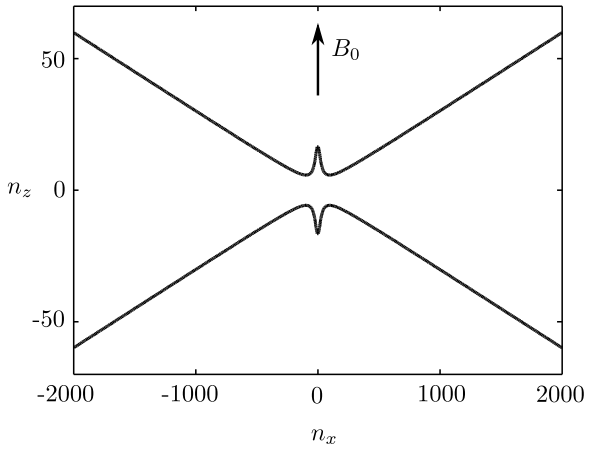

Figure 4. Cross section of the refractive index surface for a 20 kHz whistler mode wave with plasma parameters f_{ce} = 635 kHz, f_{pe} = 1.87 MHz, and f_{LHR} = 8.77 kHz. The n_x axis is normal to the scattering layers. The background magnetic field is aligned along the n_z axis. The n_x axis has been compressed in order to show the resonance cone.

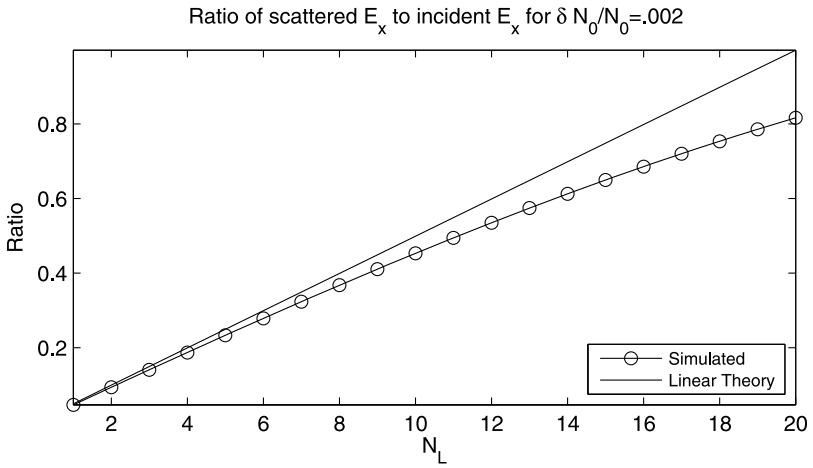

Figure 5. Ratio of the scattered QE wave amplitude E_x to the incident whistler mode wave amplitude E_x plotted for 20 wavelengths in a mild sinusoidal density perturbation.

where ψ_{res} is the resonance cone angle. The unperturbed refractive index surface is shown in Figure 4.

3.1. Sinusoidal Density Perturbations

[38] We simulated a Gaussian beam of approximately 200 km width incident on a magnetic field-aligned, sinusoidal, periodic density irregularity for a large range of parameters: θ_c = 78° to 88°, number of scattering periods N_L = 1 to 20, electron number density perturbation factor $\delta N_0/N_0$ = 0.008 to 0.256, and the variation about the matching condition's characteristic period κ = 0.9 to 1.1 (see Figure 3). Over this range of parameters, the power that can be converted into either the forward or backward QE mode is quite high, as high as α_{QE} = 40%, but for more typical cases, peaks in the range of 20%.

[39] For context, we first compare the full-wave model with the results predicted from linear scattering theory as given by (13) for a very mild density perturbation of 0.2%. The results are shown in Figure 5 and show two important trends, that the scattered wave amplitude in the QE mode shows a nearly linear increase with the number of scattering periods, and that linear scattering theory is generally valid for low values of δN_0 and low numbers of scattering periods N_L.

[40] In Figure 6, we show the reflection coefficient and QE mode conversion ratio as a function of the number of scattering periods and electron number density perturbation for beams propagating at a central incidence angle θ_c = 80° and 88°. Between 80° and 88°, the maximum conversion efficiency and overall geometry of the curve is effectively

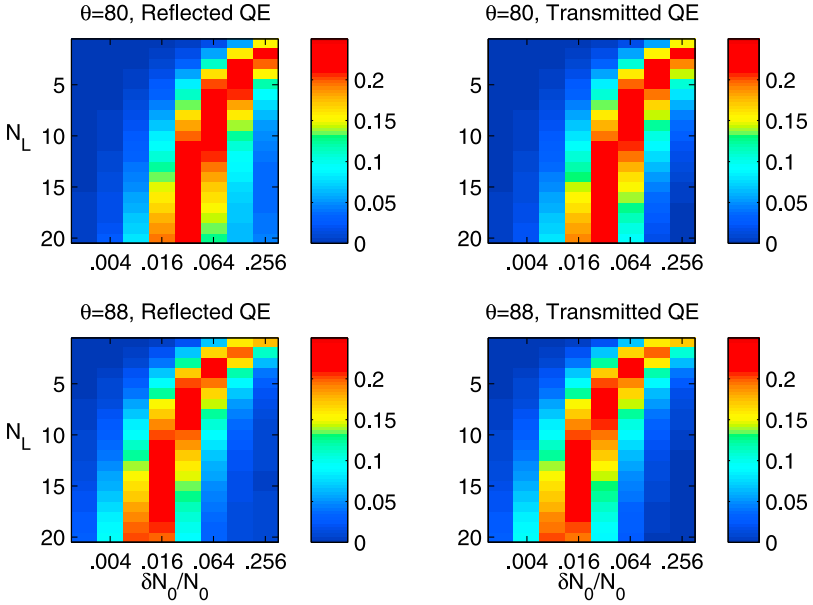

Figure 6. Intensity plot showing the forward and backward QE mode conversion efficiencies $\alpha_{QE,f}$ and $\alpha_{QE,b}$ as a function of the number of scattering periods N_L (vertical axis) and electron number density perturbation factor $\delta N_0/N_0$ (horizontal axis) for beams propagating at a central incidence angle θ_c = 80° and 88°. The spatial period of the perturbations is kept at the approximate matching condition $\lambda = \lambda_{QE}$, that is, κ = 1.

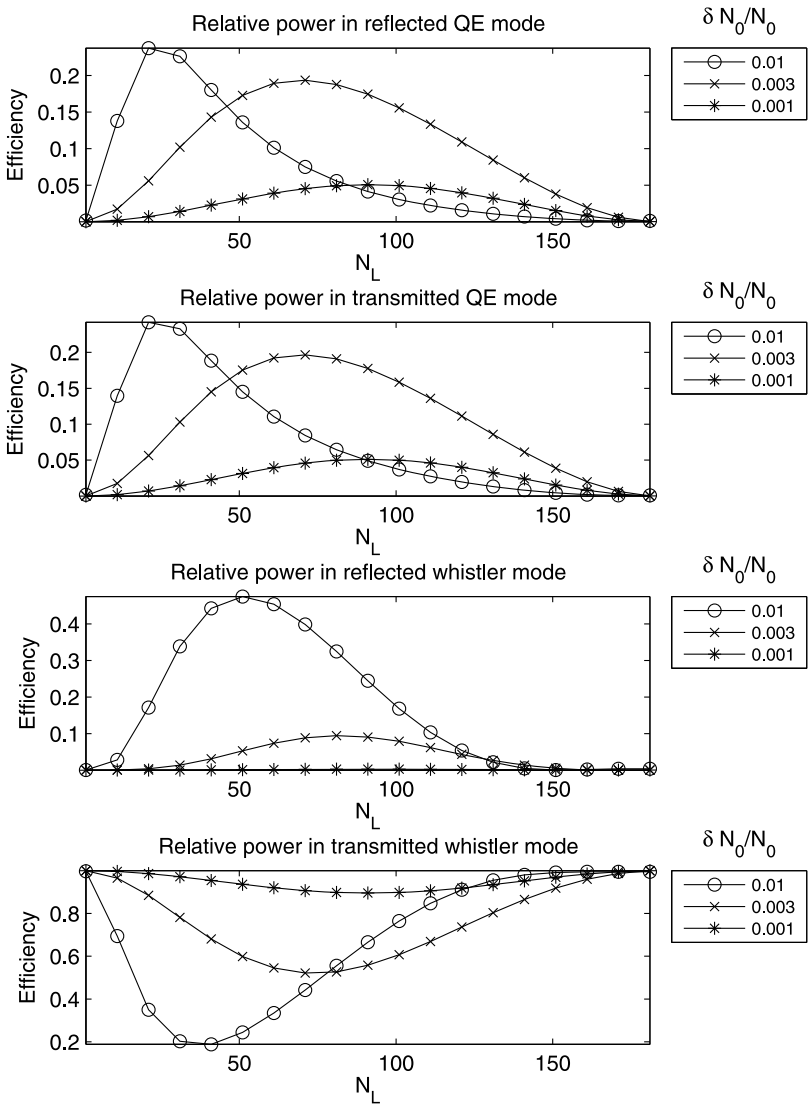

Figure 7. Plot of the total relative power in the QE and whistler modes plotted up to $N_L = 182$ for a whistler mode plane wave incident on a sinusoidal density perturbation, showing the behavior of the scattering process over many scattering periods. The spatial period of the perturbations is kept at the approximate matching condition ($\kappa = 1$). Three cases are shown, $\delta N_0/N_0 = 0.001$, $\delta N_0/N_0 = 0.003$, and $\delta N_0/N_0 = 0.01$.

unchanged; only the onset of the peak changes due to the increased interaction length at very shallow incidence. The effects of the incidence angle are essentially dominated by geometrical effects and thus predictable; we will ignore its contribution for the remainder of this paper and assume $\theta_c = 80°$. At small perturbations, the behavior is much as we would expect from linear scattering theory, but eventually the process saturates; the power converted into the QE mode increases to a maximum as either the number of layers or perturbation factor increases, and then decreases. For larger perturbations, the power decreases to zero because the matching condition cannot be maintained.

[41] Figure 7 shows a linear plot of efficiency versus the number of scattering lengths. It can be seen that all wave power is returned to the forward EM whistler mode wave when $N_i \simeq 180$. Since the wavelength of the QE waves is $\simeq$30 m, the point at which $N_i \simeq 180$ is located approximately 5 km from the initial incidence position at x = 0. This point of zero efficiency for the QE waves appears to be the same for a wide range of perturbation amplitudes. It can be seen that power from the incident EM wave initially flows into the QE waves. Power then flows from the QE waves into the reflected EM wave. The reflected EM wave is the wave labeled (b) in Figure 1. As the reflected EM wave power reaches a maximum value, the transmitted EM wave power reaches a minimum value of approximately −7 dB below its initial value.

[42] In Figure 8, we fix the number of scattering periods and show the effect of perturbing the period of the density irregularities about its nominal value expected from linear scattering theory. The log scale plot shows clearly that at low perturbations of the background electron number density, less than approximately 1 percent, there is no departure from linear scattering theory: the power converted into the QE mode is maximized when the matching condition is met. However, at higher-density perturbations, the situation

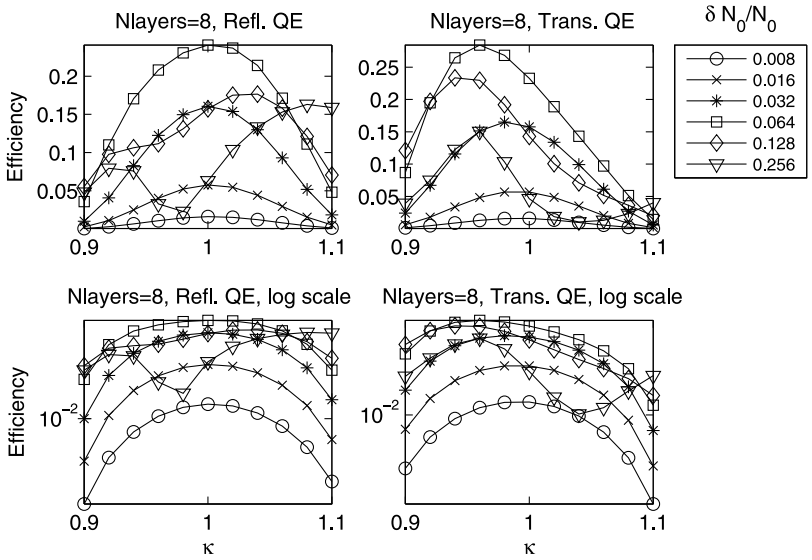

Figure 8. Log and linear scale plots of the forward and backward QE mode conversion efficiencies $\alpha_{QE,f}$ and $\alpha_{QE,b}$ for a Gaussian whistler beam incident on a periodic sinusoidal scatterer ($N_L = 8$), plotted as a function of κ, the nominal matching period's perturbation factor. Separate lines are plotted for different electron density perturbations ranging from $\delta N_0/N_0 = 0.008$ to $\delta N_0/N_0 = 0.256$.

changes. Effectively, the large number density gradient, and thus the rapidly changing refractive index, leads to a condition where the bulk of the scattered wave energy no longer constructively interferes, so the overall QE conversion efficiency is reduced. However, at high densities the peak shifts downward toward smaller κ, that is, when the spatial period of the periodic density irregularity is smaller. This can be partially explained inspecting the normal component of the refractive index as a function of the perturbation factor δN_0. As the electron number density increases, so does the normal component of the refractive index of both the EM mode and the QE mode, and thus, we would expect that the energy scattered into the QE mode would be maximized when the period of the perturbation is smaller than the "nominal" expected by only considering the background electron number density, which is precisely what we find.

[43] We illustrate the significance of this result in Figure 9. At high electron density perturbations, the peak forward QE

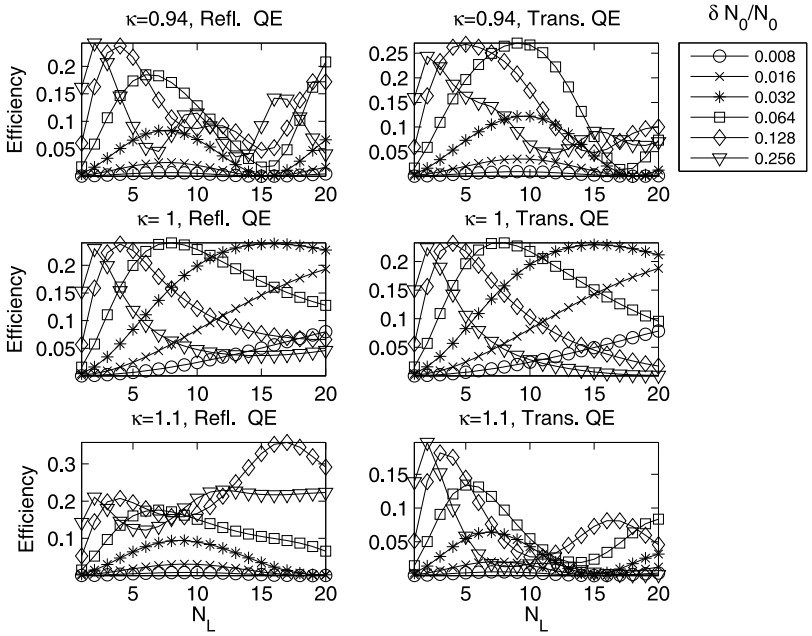

Figure 9. Plots of the forward and backward QE mode conversion efficiencies $\alpha_{QE,f}$ and $\alpha_{QE,b}$ for a Gaussian whistler beam incident on a periodic sinusoidal scatterer, plotted as a function of the number of layers N_L. Separate pairs of plots are shown for variations in the period as a function of nominal ($\kappa = 0.94$, $\kappa = 1$, and $\kappa = 1.06$).

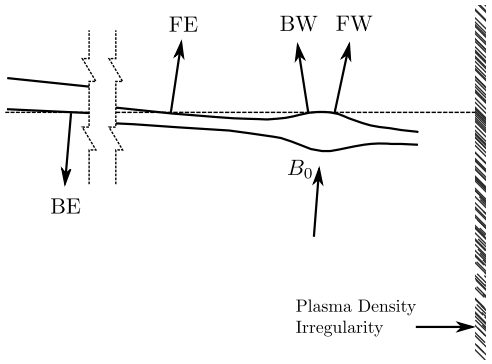

Figure 10. Illustration of the scattering problem when the background magnetic field is tilted with respect to the irregularities by an amount greater than the resonance cone angle. FW and BW denote the transmitted and reflected whistler mode wave, respectively, and FE and BE denote the transmitted and reflected quasi-electrostatic whistler mode waves, respectively.

conversion efficiency occurs at somewhat lower than the nominal scatterer period $\kappa = 1.0$, and further, the conversion efficiency continues to oscillate as a function of the number of periods N_L, no longer showing a smooth decay to zero. For the case of $\kappa = 0.94$, the maximum forward $\alpha_{\mathrm{QE,f}}$ is over 27% and at($\kappa = 1.00$), this drops to around 23%. When the period is lengthened beyond nominal ($\kappa = 1.06$), conversion efficiency rapidly decays for both the forward and backscattered QE modes. This dependence can be explained by the increase in n_x for both the whistler and QE modes as the background electron density increases, and thus the bulk of the scattered wave energy no longer constructively interferes if the factor κ is raised beyond the maximum normal component of the wavelengths of any mode supported by the medium.

[44] We point out one additional feature in Figure 9. The maximum QE conversion efficiency at a fixed $\kappa = 1.00$ is extremely insensitive to the magnitude of the electron density perturbation. For the cases tested, the maximum efficiency in both the forward or backscattered QE modes peaks in the range of 22% to 23%. While Figure 9 illustrates this well only for the cases of $\delta N_0/N_0 = 0.256$ and $\delta N_0/N_0 = 0.128$, the trend also continues for lower values of $\delta N_0/N_0$, but of course the number of layers required to attain the maximum also increases.

3.2. Layers Tilted With Respect to the Background Magnetic Field

[45] If the background magnetic field is tilted with respect to the irregularities by an angle greater than the resonance cone angle, the nature of the problem is changed. The reflected mode is now on the lower branch of the resonance cone for which the group velocity is directed toward the Earth instead of upward, as shown in Figure 10. We note that the wavelength of the forward- and backward-scattered modes can be significantly different; while the forward scattered mode may have a refractive index of a few hundred, the backward-scattered mode can be in the thousands. The consequence is that we cannot match both modes with a single sinusoidal density perturbation. While there is still a strong forward-scattered QE component, due to the refractive index mismatch, the backscattered QE wave is practically nonexistent. The forward-scattered mode, not shown here, peaks at an efficiency of approximately 30 percent for $\delta N_0/N_0 = 0.256$ and $\delta N_0/N_0 = 0.128$ and near 20 percent for $\delta N_0/N_0 = 0.064$ and $\delta N_0/N_0 = 0.032$.

3.3. Randomized Mode Sums

[46] Up to this point we have considered only a single sinusoidal plasma density irregularity in order to clearly illustrate the main properties of our system. We now consider the much more complicated situation in which the plasma density irregularities are made up of multiple spatial Fourier modes of different amplitude, wave number, and phase, as shown below,

$$N(x) = N_0 + \sum_{i=1}^{M} A_i \cos(k_i x - \phi_i), \tag{25}$$

where A_i is the mode amplitude, k_i is mode wave number, and ϕ_i is the mode phase. We consider A_i, k_i, and ϕ_i in (25) to be random variables. For feasibility, we limit ourselves to a finite number of modes M, then solve the scattering problem for 400000 random trials, where the number of modes is drawn from a uniform distribution U(1,121), the total scattering region length from U(λ_0, 11λ_0), the mode amplitudes A_i from U(0, 0.5/M), and phases ϕ_i from U(0, 2π).

[47] The variable k_i is related to the mode period variation parameter κ_i through the equation, $k_i = 2\pi/\kappa_i\lambda_0$. In the first set of trials, we fix κ_i at the value $\kappa_i = 1$, and in the second, κ_i is drawn from a lognormal distribution Log-$\mathcal{N}(\mu, \sigma)$. Due to the enormity of the data, we summarize the results in a single plot that shows, for a fixed relative probability of occurrence, the total relative power in both upgoing QE modes, or more precisely, we plot the maximum value of α such that

$$\mathbf{prob}(\alpha_{\mathrm{QE,f}} + \alpha_{\mathrm{QE,b}} \geq \alpha) \geq p_0, \tag{26}$$

for some fixed value of p_0, e.g., $p_0 = 0.25$. The results are shown in Figure 11. Typical mode conversion efficiencies still peak at approximately 50%.

3.4. Randomized Coherence Length

[48] The coherence length for the scattering of QE and EM waves in our system may be significantly less than the actual extent of the irregularities along the x axis. For example, the group velocity direction of the excited QE waves is approximately perpendicular to the resonance cone, which in our case has a half angle of 88.29°. Thus for every kilometer the QE waves propagate along the x axis perpendicular to $\mathbf{B}_0$, they will propagate upward approximately 30 km along $\mathbf{B}_0$. The magnitude of the background plasma density and the magnitude and direction of $\mathbf{B}_0$ will change over this 30 km distance, and the wavelengths of the QE and EM waves will change in response to these changes in $N_0(r)$ and $\mathbf{B}_0$. Consequently the matching condition of (16) may apply only over a limited altitude range δs, which corresponds to the propagation distance δx_c along the x axis. The quantity δx_c can then be thought of as a coherence length for the EM and QE waves scattering from the irregularities.

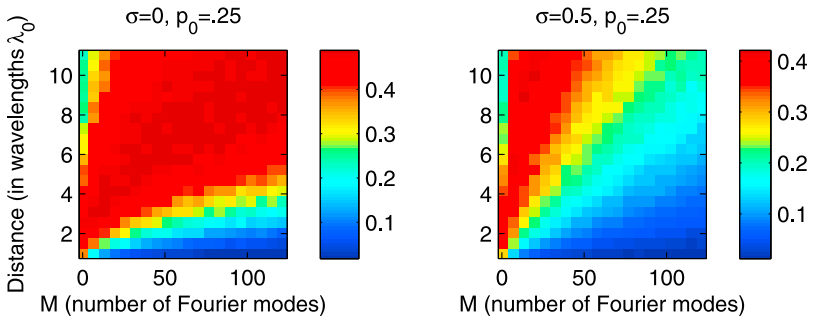

Figure 11. The total QE mode conversion efficiency (the maximum value of α such that $\text{prob}(\alpha_{\text{QE,total}} \geq \alpha) \geq p_0$), plotted for a fixed probability of occurrence $p_0 = 0.25$. The horizontal axis is the total number of Fourier modes (M) and the vertical axis is the distance normalized by the nominal scattering wavelength λ_0. Shown are two cases: on the left is the case in which $\kappa_i = 1$ exactly, on the right, κ_i is drawn from a distribution log-$\mathcal{N}(\mu = 0, \sigma = 0.5)$.

[49] The energy transfer between the QE and EM waves can be significantly affected by the value of δx_c. This can be seen from Figure 7, where if δx_c is less than 50 wavelengths, the wave energy initially transferred to the QE waves can no longer be returned to the EM waves in a single scattering event.

[50] Within the context of (25), we define the coherence length to be the distance over which the ϕ_i values are constant. We assume that the density irregularities have some characteristic periodic scale, but we allow the average coherence length to vary. We conduct the simulation much as in the last section, drawing 400,000 random samples over the space of interest, but fix $\kappa = 1$ and draw the total length of the scattering region from $U(\lambda_0, 16\lambda_0)$. The region is divided into fractional segments over which the phase is kept constant. The average width of these segments is drawn from a uniform distribution U(0, 1), and the phase of each segment is drawn from $U(0, 2\pi)$. Results are shown in Figure 15. The plotted quantity is the same as that plotted in Figure 11.

[51] The maximum extent of the irregularities along the x axis in Figure 15 is 16 wavelengths, or approximately 500 m. Taking the group velocity direction into account, the QE waves propagate upward approximately 15 km while propagating these 500 m.

[52] Of particular note is that the total QE conversion efficiency obtained can be as high as 80%, a result that exceeds that of all of the smooth sinusoidal perturbations considered earlier. The probability of occurrence over these parameters is small, less than 2 percent, but is nonetheless possible. The figures also show a trend toward decreasing dependence on the length of the scattering region as the coherence length grows very small. That is, partly incoherent scatter is potentially a robust mechanism for scattering into the QE mode.

3.5. Fixed Coherence Length

[53] Thus far we have considered mode conversion efficiency over propagation distances of approximately 500 m perpendicular to $\mathbf{B}_0$ and 15 km parallel to $\mathbf{B}_0$. To investigate the QE mode conversion efficiency over larger propagation distances, we fix the coherence length and calculate the mode conversion efficiency as a function of the number of coherence lengths over which the waves have propagated. We consider two fixed coherence lengths, $\delta x_c = 3\lambda_0$ and $\delta x_c = 15\lambda_0$. The value of the wave phase discontinuity between adjoining coherence length sections is taken from $U(0, 2\pi)$. The results are shown in Figures 12 and 13. In each case the maximum propagation distance is approximately 5 km perpendicular to $\mathbf{B}_0$ and 150 km parallel to $\mathbf{B}_0$.

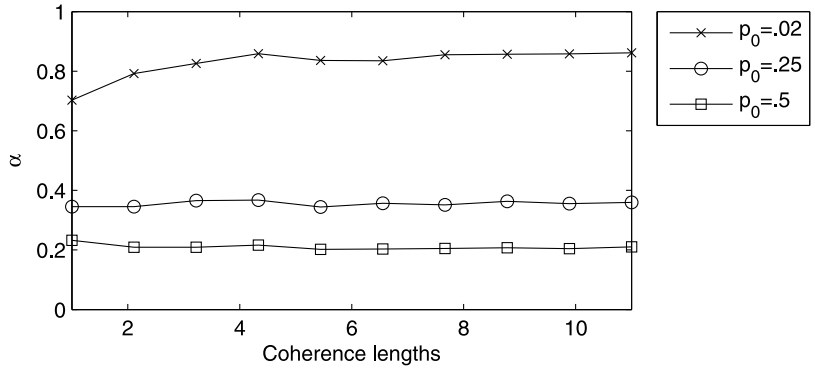

Figure 12. The total QE mode conversion efficiency (the maximum value of α such that $\text{prob}(\alpha_{\text{QE,total}} \geq \alpha) \geq p_0$), plotted for $p_0 = 0.02$, $p_0 = 0.25$, and $p_0 = 0.5$. The coherence length is fixed at $15\lambda_0$ and the phase discontinuity between adjoining sections is drawn from $U(0, 2\pi)$. The horizontal axis is the total number of coherence lengths.

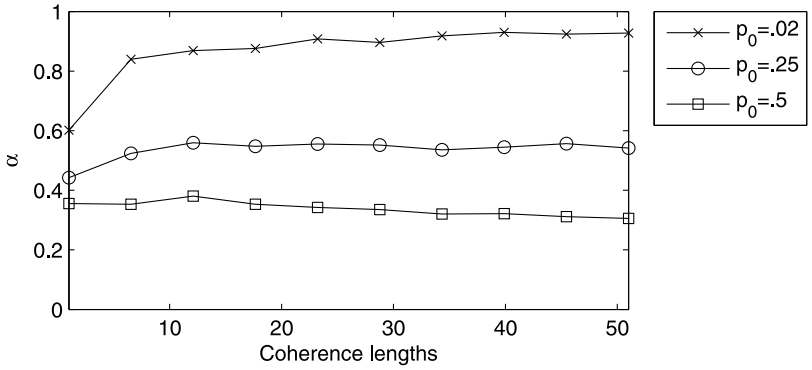

Figure 13. The total QE mode conversion efficiency (the maximum value of α such that prob($\alpha_{QE,total} \geq \alpha$) $\geq p_0$), plotted for $p_0 = 0.02$, $p_0 = 0.25$, and $p_0 = 0.5$. The coherence length is fixed at $3\lambda_0$, and the phase discontinuity between adjoining sections is drawn from $U(0, 2\pi)$. The horizontal axis is the total number of coherence lengths.

Figure 12 treats the case of $\delta x_c = 15\lambda_0$. It can be seen that the total QE mode conversion efficiency is not a strong function of propagation distance and that the most probable values of efficiency lie in the range 0.2–0.35. However, efficiency values as high as 0.85 are possible.

[54] Figure 13 treats the case of $\delta x_c = 3\lambda_0$. It can be seen that the total QE mode conversion efficiency is not a strong function of propagation distance after approximately 5 coherence lengths and that the more probable values of total efficiency lie in the range of 0.3–0.5. Thus comparing Figures 12 and 13 we see that the efficiency values are larger when the coherence length is smaller. It is notable in Figure 13 that the efficiency can reach values larger than 0.9, albeit at a very low probability in our model. A total QE efficiency of 0.9 represents a power loss of 10 dB for the input EM wave.

[55] In an attempt to identify the conditions under which the total QE mode conversion efficiency can reach large values equal to, or larger than, 0.85, we examined all of our cases for which this constraint was true and for each plotted the values of the phase shift ϕ_i between each fixed coherence length. The results are shown in Figure 14. It can be seen that the intercoherence length phase shifts for these cases predominantly have values near 45°, and −170°, or approximately $\pi/4$ and $-\pi$. A phase shift of π between adjacent coherence lengths means that the sinusoidal density perturbations in the two sections will be completely out of phase with respect to each other. This circumstance may limit the conversion of QE waves into EM waves, resulting in a larger overall power loss for the EM wave. It is not clear why a phase shift of $\pi/4$ would result in a larger power loss for the EM waves. However, since we are dealing with a four wave interaction, a phase shift of $\pi/4$ between sections may possibly result in a phase shift of π between the QE and EM waves.

3.6. Landau Damping, Cyclotron Damping, and Collisional Losses

[56] We have ignored the effects of Landau damping, cyclotron damping, and collisional losses throughout this paper. We now show that their effects are negligible over the length scales considered (Figure 15).

[57] We solve equation (3.9) of *Kennel* [1966], corrected for a minor typographical error noted by *Chen et al.* [2009] for the electron cyclotron and Landau resonances to find the temporal damping rate ω_i and then find the spatial damping rate k_i by the relation of *Brinca* [1972],

$$\omega_i = \vec{k_i} \cdot \vec{v_g}. \tag{27}$$

The hot electron distribution is based on an observation-fitted suprathermal distribution from [*Bell et al.*, 2002]

$$f_a(v) = a/v^4 - b/v^5 + c/v^6, \tag{28}$$

where $a = 4.9 \cdot 10^5/(\text{cm}^2\ \text{s})$, $b = 8.3 \cdot 10^{14}/(\text{cm}\ \text{s}^2)$, and $c = 5.4 \cdot 10^{23}/(\text{s}^3)$.

[58] Collisional losses are incorporated in the standard way, e.g., *Stix* [1962]. We assume the collision frequency is a relatively conservative 1 s^{-1}. The results are summarized in Figure 16, where we see that over the plotted range, both collisional losses and thermal losses are negligible. Collisional losses are a few orders of magnitude higher, but rapidly drop off as the altitude increases, so neither can be a considered significant source of loss.

4. Conclusions

[59] We have used both a perturbation solution of Maxwell's equations and a recently developed layered media full-wave model to investigate linear mode conversion from EM whistler mode waves to QE whistler mode waves in the presence of small-scale magnetic field-aligned plasma density irregularities. In the simplest case of a single time invariant sinusoidal magnetic field-aligned density irregularity and an incident Gaussian beam of VLF whistler mode waves, we have shown that when the spatial wavelength of the single irregularity is approximately equal to the wavelength of the QE waves significant excitation of QE waves can occur. In particular, we have shown that significant amounts of incident whistler mode energy can be scattered into the QE modes by this mechanism, peaking at over 50% conversion efficiency over a wide range of parameters. Further, we have shown that in the presence of significant plasma density gradients, the peak conversion efficiency

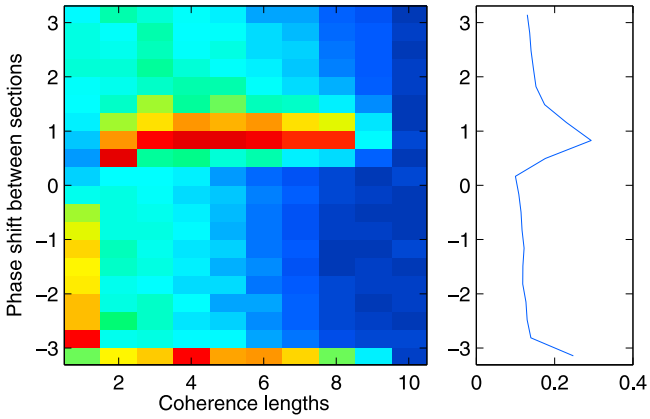

Figure 14. Distribution showing configurations with large (greater than 0.85) total QE mode conversion efficiencies, binned over the relative phase shift between coherent segments (y axis) and the total number of coherent segments (x axis) each with coherence length $\delta x_c = 15\lambda_0$.

shows a strong sensitivity to the characteristic period of the irregularity, with the peak occurring for scattering periods slightly less than that expected by a simple scattering model (e.g., distributed Bragg reflectors). In the much more complicated case in which the irregularities consist of multiple Fourier components with random values of amplitude, wave number, and phase, we show that 50% conversion efficiency is still possible. In addition in cases in which the coherence length of the scattering process is less than the width of the irregularity region, we have shown that robust QE wave excitation is possible, with conversion efficiency in excess of 85%.

[60] Although we have concentrated on the power lost by the incident EM whistler mode wave in exciting the QE waves, the incident EM wave also loses power to the reflected EM whistler mode wave. This is the wave labeled (b) in Figure 1. Since the wave normal angles of the incident and reflected EM waves are different, they will propagate in different directions. This divergence can be envisioned as a spreading loss for the incident EM wave.

[61] We note that for magnetic field-aligned density irregularities, the linear scattering mechanism described in this paper only strictly applies for frequencies above the lower hybrid resonance frequency. At frequencies below the lower hybrid resonance frequency, the refractive index surface topology changes from open to closed, and thus it is no longer possible to excite short-wavelength modes from magnetic field aligned density irregularities. However, we note that if the irregularities are tilted with respect to the magnetic field, it is still possible to excite short-wavelength modes in a manner nearly identical to that shown in Figure 10. In addition, purely evanescent modes may be excited if the plasma density gradients are high enough.

[62] In our work we have concentrated on linear mode coupling as a power loss for electromagnetic whistler mode waves. However, recently *Mishin et al.* [2010] have examined nonlinear interactions driven by intense VLF pump waves in the topside ionosphere over the 1 MW North West Cape (NWC) VLF transmitter in Australia. The authors suggest that these nonlinear interactions may be responsible for additional energy losses of the NWC signals as they propagate upward through the strongly heated ionosphere. This type of power loss would not appear to apply to less powerful VLF transmitters, such as NPM, over which no signs of strong ionospheric heating are generally observed.

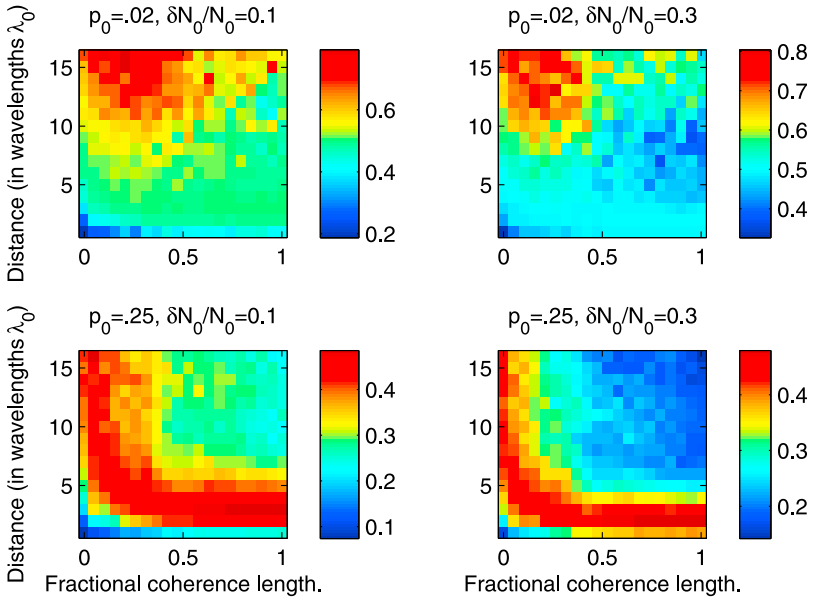

Figure 15. The total QE mode conversion efficiency (the maximum value of α such that prob $(\alpha_{QE,total} \geq \alpha) \geq p_0$) as a function of the fractional coherence length, which is the fraction of the total length of the scattering region over which the phase is held constant (horizontal axis), and the distance normalized by the nominal scattering wavelength λ_0 (vertical axis). Shown are two cases, $\delta N_0/N_0 = 0.1$ and $\delta N_0/N_0 = 0.3$, plotted at $p_0 = 0.02$ and $p_0 = 0.25$.

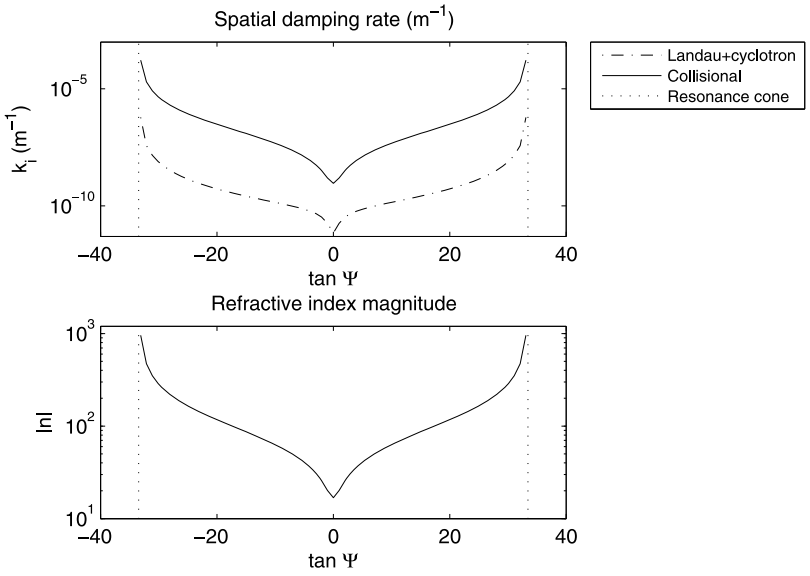

Figure 16. Spatial damping rate due to collisional and thermal (cyclotron and Landau resonances) losses plotted as a function of tanΨ. The vertical dashed lines denote the location of the resonance cone angle. (bottom) We plot up to a refractive index magnitude $|n|$ of approximately 1000 (shown for reference). (top) The losses due to collisions and those due to thermal effects as separate lines.

Thus both linear and nonlinear interactions may need to be invoked to explain the pervasive VLF wave power deficit reported by *Starks et al.* [2008].

[63] In summary, for short propagation paths, we predict power losses ranging from −3 dB (25% probability) to −7 dB (2% probability). We predict the power loss of EM whistler mode waves propagating through longer propagation paths can be as high as −4 dB (at 25% probability) to over −10 dB (2% probability). We conclude that the power loss in EM whistler mode waves due to excitation of QE whistler mode waves in regions containing small-scale plasma density irregularities may account for a portion of the −20 dB EM wave power deficit reported by *Starks et al.* [2008].

[64] **Acknowledgments.** The authors were supported by the Office of Naval Research under Prime Award N000140710789 to the University of Maryland with subcontract Z882802 to Stanford and under grant N00014-09-1-0034-P00003.

[65] Robert Lysak thanks Michael Starks and another reviewer for their assistance in evaluating this paper.

References

Abel, B., and R. M. Thorne (1998), Electron scattering loss in Earth's inner magnetosphere: 1. Dominant physical processes, *J. Geophys. Res.*, *103*(A2), 2385–2396, doi:10.1029/97JA02919.

Balanis, C. A. (1989), *Advanced Engineering Electromagnetics*, John Wiley, New York.

Bell, T. F., and H. D. Ngo (1988), Electrostatic waves stimulated by coherent VLF signals propagating in and near the inner radiation belt, *J. Geophys. Res.*, *93*(A4), 2599–2618, doi:10.1029/JA093iA04p02599.

Bell, T. F., and H. D. Ngo (1990), Electrostatic lower hybrid waves excited by electromagnetic whistler mode waves scattering from planar magnetic field-aligned plasma density irregularities, *J. Geophys. Res.*, *95*(A1), 149–172, doi:10.1029/JA095iA01p00149.

Bell, T. F., U. S. Inan, J. P. Katsufrakis, and H. G. James (1983), The apparent spectral broadening of VLF transmitter signals during transionospheric propagation, *J. Geophys. Res.*, *88*(A6), 4813–4840, doi:10.1029/JA088iA06p04813.

Bell, T. F., U. S. Inan, V. S. Sonwalkar, and R. A. Helliwell (1991), DE-1 observations of lower hybrid waves excited by VLF whistler mode waves, *Geophys. Res. Lett.*, *18*(3), 393–396, doi:10.1029/90GL02598.

Bell, T. F., U. S. Inan, J. Bortnik, and J. D. Scudder (2002), The Landau damping of magnetospherically reflected whistlers within the plasmasphere, *Geophys. Res. Lett.*, *29*(15), 1733, doi:10.1029/2002GL014752.

Bell, T. F., U. S. Inan, M. Platino, J. S. Pickett, P. A. Kossey, and E. J. Kennedy (2004), CLUSTER observations of lower hybrid waves excited at high altitudes by electromagnetic whistler mode signals from the HAARP facility, *Geophys. Res. Lett.*, *31*, L06811, doi:10.1029/2003GL018855.

Bell, T. F., U. S. Inan, D. Piddyachiy, P. Kulkarni, and M. Parrot (2008), Effects of plasma density irregularities on the pitch angle scattering of radiation belt electrons by signals from ground based VLF transmitters, *Geophys. Res. Lett.*, *35*, L19103, doi:10.1029/2008GL034834.

Brinca, A. L. (1972), On the stability of obliquely propagating whistlers, *J. Geophys. Res.*, *77*(19), 3495–3507, doi:10.1029/JA077i019p03495.

Chen, L., J. Bortnik, R. M. Thorne, R. B. Horne, and V. K. Jordanova (2009), Three-dimensional ray tracing of VLF waves in a magnetospheric environment containing a plasmaspheric plume, *Geophys. Res. Lett.*, *36*, L22101, doi:10.1029/2009GL040451.

Groves, K. M., M. C. Lee, and S. P. Kuo (1988), Spectral broadening of VLF radio signals traversing the ionosphere, *J. Geophys. Res.*, *93*(A12), 14,683–14,687, doi:10.1029/JA093iA12p14683.

Harker, K. J., and F. W. Crawford (1969), Nonlinear interaction between whistlers, *J. Geophys. Res.*, *74*(21), 5029–5040, doi:10.1029/JA074i021p05029.

Imachi, T., I. Nagano, S. Yagitani, M. Tsutsui, and H. Matsumoto (2000), Effective lengths of the dipole antennas aboard Geotail spacecraft, *Proc. ISAP*, *2000*, 819–822.

James, H. G. (2006), Dipole Measurements of Waves in the Ionosphere, in *Geospace Electromagnetic Waves and Radiation*, *Lect. Notes Phys.*, vol. 687, edited by J. W. Labelle and R. A. Treumann, pp. 191–210, Springer, Berlin.

James, H. G., and T. F. Bell (1987), Spin modulation of spectrally broadened VLF signals, *J. Geophys. Res.*, *92*(A7), 7560–7568, doi:10.1029/JA092iA07p07560.

Kennel, C. (1966), Low-frequency whistler mode, *Phys. Fluids*, *9*, 2190–2202, doi:10.1063/1.1761588.

Lehtinen, N. G., and U. S. Inan (2008), Radiation of ELF/VLF waves by harmonically varying currents into a stratified ionosphere with application to radiation by a modulated electrojet, *J. Geophys. Res.*, *113*, A06301, doi:10.1029/2007JA012911.

Lehtinen, N. G., and U. S. Inan (2009), Full-wave modeling of transionospheric propagation of VLF waves, *Geophys. Res. Lett.*, *36*, L03104, doi:10.1029/2008GL036535.

Millan, R. M., and R. M. Thorne (2007), Review of radiation belt relativistic electron losses, *J. Atmos. Solar-Terr. Phys.*, *69*, 362–377, doi:10.1016/j.jastp.2006.06.019.

Mishin, E. V., M. J. Starks, G. P. Ginet, and R. A. Quinn (2010), Nonlinear VLF effects in the topside ionosphere, *Geophys. Res. Lett.*, *37*, L04101, doi:10.1029/2009GL042010.

Ngo, H. D. (1989), Electrostatic Waves Stimulated by VLF Whistler Mode Waves Scattering from Magnetic-field-aligned Plasma Density Irregularities, Ph.D. thesis, Stanford Univ., Palo Alto, Calif.

Santolík, O., M. Parrot, and F. Lefeuvre (2003), Singular value decomposition methods for wave propagation analysis, *Radio Sci.*, *38*(1), 1010, doi:10.1029/2000RS002523.

Sonwalkar, V. S., and U. S. Inan (1986), Measurements of Siple transmitter signals on the DE 1 satellite: Wave normal direction and antenna effective length, *J. Geophys. Res.*, *91*(A1), 154–164, doi:10.1029/JA091iA01p00154.

Starks, M. J., R. A. Quinn, G. P. Ginet, J. M. Albert, G. S. Sales, B. W. Reinisch, and P. Song (2008), Illumination of the plasmasphere by terrestrial very low frequency transmitters: Model validation, *J. Geophys. Res.*, *113*, A09320, doi:10.1029/2008JA013112.

Stix, T. H. (1962), *The Theory of Plasma Waves*, McGraw-Hill, New York.

Tanaka, Y., M. Hayakawa, D. Lagoutte, F. Lefeuvre, and S. Tajima (1987), Spectral broadening of VLF transmitter signals and sideband structure observed on Aureol 3 satellite at middle latitudes, *J. Geophys. Res.*, *92* (A7), 7551–7559, doi:10.1029/JA092iA07p07551.

Titova, E. E., V. I. Di, V. E. Iurov, O. M. Raspopov, V. I. Trakhtengerts, F. Jiricek, and P. Triska (1984), Interaction between VLF waves and the turbulent ionosphere, *Geophys. Res. Lett.*, *11*(4), 323–326, doi:10.1029/GL011i004p00323.

T. F. Bell, F. R. Foust, U. S. Inan, and N. G. Lehtinen, Department of Electrical Engineering, Stanford University, Packard Building, 350 Serra Mall, Stanford, CA 94305, USA. (ffoust@stanford.edu)